

Observation of strong spin–orbital entanglement in Sr_2RuO_4 by spin-resolved ARPES

C. N. Veenstra,¹ Z. -H. Zhu,¹ M. Raichle,¹ B. M. Ludbrook,¹ A. Nicolaou,^{1,2} B. Slomski,^{3,4} G. Landolt,^{3,4}
S. Kittaka,^{5,6} Y. Maeno,⁵ J. H. Dil,^{3,4} I. S. Elfimov,^{1,2} M. W. Haverkort,^{1,2,7} and A. Damascelli^{1,2,*}

¹Department of Physics & Astronomy, University of British Columbia, Vancouver, British Columbia V6T 1Z1, Canada

²Quantum Matter Institute, University of British Columbia, Vancouver, British Columbia V6T 1Z4, Canada

³Physik-Institut, Winterthurerstrasse 190, Universität Zürich-Irchel, CH-8057 Zürich, Switzerland

⁴Swiss Light Source, Paul Scherrer Institut, CH-5232 Villigen PSI, Switzerland

⁵Department of Physics, Graduate School of Science, Kyoto University, Kyoto 606-8502, Japan

⁶Institute for Solid State Physics, University of Tokyo, Kashiwa, Chiba 277-8581, Japan

⁷Max Planck Institute for Solid State Research, Heisenbergstraße 1, 70569 Stuttgart, Germany

(Dated: March 25, 2013)

After a flurry of experimental activity [1–5], Sr_2RuO_4 has become a hallmark candidate for spin-triplet chiral p -wave superconductivity, the electronic analogue of superfluid ^3He [6]. However, despite the apparent existence of such a pairing, some later experiments [7–9] do not fully support this conclusion, as they cannot be explained within a theoretical model using spin-triplet superconductivity alone [10]. A resolution might come from the inclusion of spin–orbit coupling, which has been conjectured to play a key role in the low energy electronic structure [11]. Using circularly polarized light combined with spin- and angle-resolved photoemission spectroscopy, we directly measure the value of the effective spin–orbit coupling to be 130 ± 30 meV. This is even larger than theoretically predicted and comparable to the energy splitting of the d_{xy} and $d_{xz,yz}$ orbitals around the Fermi surface, resulting in a strongly momentum-dependent entanglement of spin and orbital character. As a consequence, the classification of the Cooper pairs in terms of singlets or triplets fundamentally breaks down, necessitating a description of the unconventional superconducting state of Sr_2RuO_4 beyond these pure spin eigenstates.

With the discovery of topological insulators [12], as well as relativistic Mott-insulating behavior in $5d$ transition metal oxides [13, 14], there has been a renaissance in the study of spin–orbit (SO) coupling and the novel phenomena it might induce in complex materials. By mixing the canonical spin eigenstates, the relativistic SO interaction might also offer a resolution to conflicting experiments regarding the nature of the superconducting pairing in Sr_2RuO_4 . In fact, SO coupling’s major role in determining the electronic band structure – as indicated by ab initio density functional theory results [11] – suggests that its consideration may indeed be important when describing superconductivity as well; this could play a fundamental role beyond simply lifting the degeneracy of competing pairing states [11, 15–18].

However, thus far, the experimental investigation of SO coupling’s effects on the electronic structure of Sr_2RuO_4 has been limited to the comparison of band calculations against angle-resolved photoemission spectroscopy (ARPES) [11, 19, 20] – no success has been obtained in observing experimentally either the strength of SO coupling or its implications for the mixing between spin and orbital descriptions. Here we probe this directly by performing spin-resolved ARPES with circularly-polarized light, by using the angular momentum inherent in each photon, along with electric-dipole selection rules, to generate spin-polarized photoemission from the SO mixed states. Combined with a novel spin- and orbitally-resolved ab initio-based tight-binding (TB) modelling of the electronic structure (Methods), these results demonstrate the presence of a non-trivial *spin–*

orbital entanglement over much of the normal-state Fermi surface, i.e. with no simple way of factoring the band states into the spatial and spin sectors.

In Sr_2RuO_4 the calculated effective SO coupling is comparatively small ($\zeta_{\text{eff}} \sim 90$ meV at the Γ point) with respect to the bandwidth (~ 3 eV) of the Ru- t_{2g} orbitals, which define the α , β , and γ conduction bands. Nevertheless its influence always becomes important whenever bands would be degenerate in the absence of SO, either by symmetry or accidentally. This happens at several places in the three-dimensional (3D) Brillouin zone, as demonstrated in Fig. 1(a,b) where we show a comparison of the ab initio-TB band structure and Fermi surface calculated both with (color) and without (black) SO coupling included (Methods). In the absence of SO, by symmetry the d_{xz} and d_{yz} bands would be degenerate along the entire k_z momentum path from Γ to Z [Fig. 1(a)]. Additionally, there are accidental degeneracies along the $k_z = 0$ path from Γ to X, where the bands of $d_{xz,yz}$ and d_{xy} character all cross at momenta near $(2\pi/3, 2\pi/3)$ – the exact location of which varies with k_z but often occurs at the Fermi level [Fig. 1(a,b)]. At all these locations SO coupling naturally leads to a splitting [Fig. 1(a,b)] and mixing of the orbital character [Fig. 1(c)] for all three bands.

Interestingly, the effects of SO coupling are not limited to the regions around the non-relativistic degeneracies as, despite the large bandwidth, the Ru- t_{2g} bands are often separated by energies small compared to the SO interaction. The predicted importance of the SO interaction can be directly visualized via the expectation value of $\vec{l} \cdot \vec{s}$ from

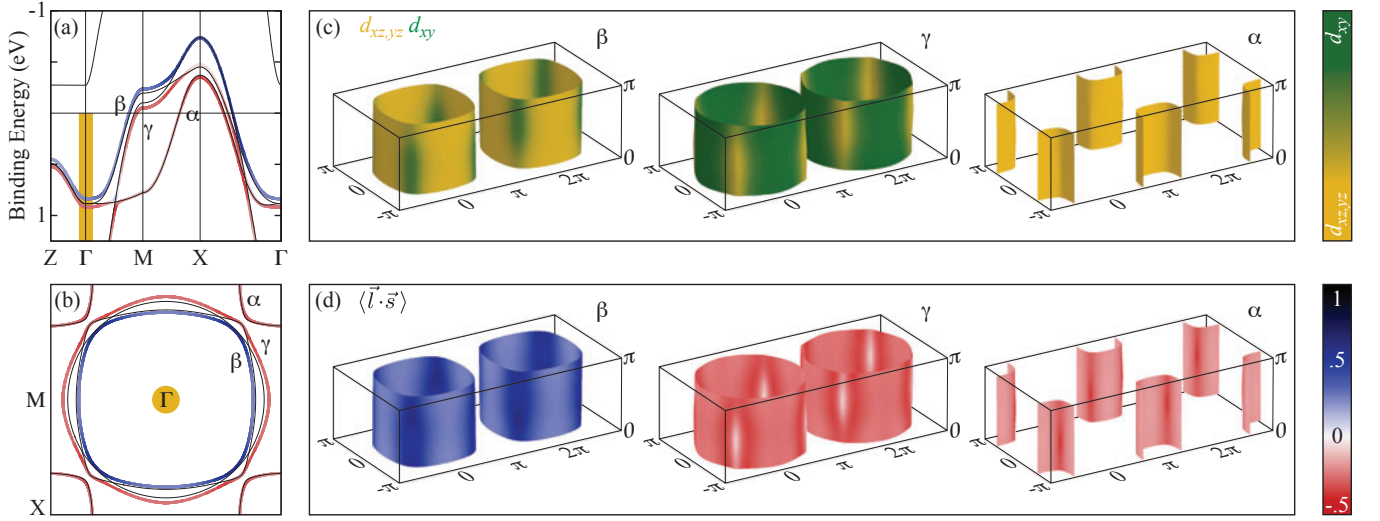


FIG. 1: **Effect of SO coupling on the band dispersion and Fermi surface of Sr_2RuO_4 .** (a) Band structure along the high-symmetry directions, and (b) $k_z = 0$ Fermi surface, calculated both without (thin black) and with (thick, color-coded to show $\langle \vec{l} \cdot \vec{s} \rangle$) the inclusion of SO coupling; at the Γ point, the latter gives rise to a $\zeta_{\text{eff}} \sim 90$ meV splitting [note that $Z \equiv (0, 0, \pi/c)$, $\Gamma \equiv (0, 0, 0)$, $M \equiv (\pi/a, 0, 0)$, $X \equiv (\pi/a, \pi/a, 0)$]. (c,d) 3D Fermi surface sheets color-coded to show (c) orbital character and (d) the expectation value $\langle \vec{l} \cdot \vec{s} \rangle$; the extended zone scheme is used to illustrate the conventional Brillouin zone in the body-centered tetragonal unit cell of Sr_2RuO_4 . The energy and momentum location of the spin-resolved ARPES spectra shown in Fig. S3 is marked in yellow in panels (a) and (b).

our ab initio-TB modelling, with \vec{l} and \vec{s} being the orbital and spin angular momentum operators. A non-zero value of $\langle \vec{l} \cdot \vec{s} \rangle$ indicates complex orbital eigenstates that can be entangled with the spin. In this case, the wavefunction cannot be factorized into independent spin and orbital parts, as would be possible for a fully quenched angular momentum (for which $\langle \vec{l} \cdot \vec{s} \rangle = 0$). The calculated $\langle \vec{l} \cdot \vec{s} \rangle$ is shown in Fig. 1 for the high-symmetry dispersion (a), $k_z = 0$ Fermi surface (b), and around the 3D Fermi sheets (d). This suggests SO coupling is important in Sr_2RuO_4 on almost the entire three-sheet Fermi surface [21].

In order to probe the resulting internal spin-orbital structure of the band states, we turn to spin-resolved ARPES with circularly polarized light: with this technique the circular polarization of the light couples to the angular momentum of the states measured at a given k point, while the spin is resolved directly. A similar approach, albeit without the angular and energy resolution needed to resolve states near the Fermi level, has been used previously to generate spin-polarized photoemission from materials without a net magnetization, such as GaAs [22] and Ca_2RuO_4 [23]. Here, exploiting the electron-dipole selection rules for photoemission from initial states carefully selected via spin-resolved ARPES, we will – for the first time – directly probe the internal SO structure of the wavefunction for these critical near-Fermi-level states. This study will be done at ~ 40 K, thus in the normal state well above $T_c \simeq 1.5$ K.

To apply this technique on Sr_2RuO_4 we study the SO splitting at the Γ point, $\vec{k} = (0, 0, 0)$; this location is high-

lighted in Fig. 1(a,b). As explained below, this selects both the experimental geometry and initial-state wavefunctions that are the most straightforward to understand, facilitating the direct measurement of both the SO interaction strength and the complex nature of the wavefunction. At this k -point, non-relativistic band structure calculations predict two degenerate bands of d_{xz} and d_{yz} character, with the d_{xy} band far enough away that it can be ignored (i.e., at about 1.8-2.3 eV higher binding energy, depending on the k_z value). Here SO breaks the degeneracy by hybridizing these bands to form two states with a splitting of $\zeta_{\text{eff}} \sim 90$ meV: a lower binding-energy state with z -components of orbital and spin angular momentum *parallel* $|d_{-1z}^\downarrow, d_{+1z}^\uparrow\rangle$, and a higher binding-energy state where they are *antiparallel* $|d_{-1z}^\uparrow, d_{+1z}^\downarrow\rangle$. Here \uparrow_z represents spin, $d_{+1z} \equiv \sqrt{1/2}(-d_{xz} - id_{yz})$ has $m_l = 1$, while $d_{-1z} \equiv \sqrt{1/2}(d_{xz} - id_{yz})$ has $m_l = -1$. Optical selection rules for the initial-to-final-state excitation with circularly polarized light dictate that both $\Delta\ell = \pm 1$ and $\Delta m_l = \pm 1$. For d orbitals the change in ℓ will strongly favour the $d \rightarrow p$ over $d \rightarrow f$ transitions, owing to the cross-section at the photon energies used (24 and 56 eV); the change in m_l will depend on the circular polarization of the photon being right (\oplus) or left (\ominus). When a \oplus (\ominus) photon is absorbed by the lower binding-energy *parallel* $|d_{-1z}^\downarrow, d_{+1z}^\uparrow\rangle$ state, m_{l_z} must increase (decrease) by one; but since $|m_{l_z}| = 2$ is forbidden in the strongly favoured p transition, electrons from the

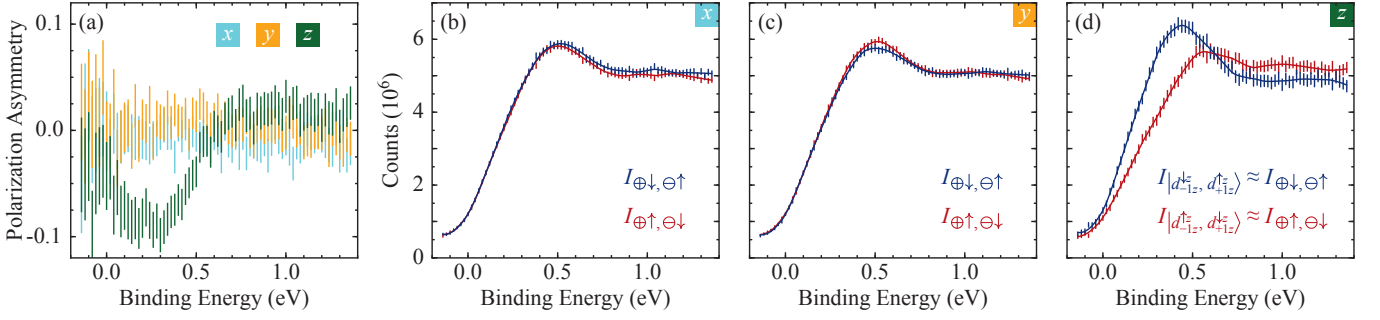


FIG. 2: **Spin-resolved ARPES results on Sr_2RuO_4 at the Γ point.** (a) Measured polarization asymmetry of the photoemitted electrons, and (b-d) corresponding spin-resolved ARPES intensities relative to the x , y , and z crystal axes obtained with right (\oplus) or left (\ominus) circularly polarized 24 eV photons at the Γ point, as highlighted in Fig. 1. Note that, for the z direction (d), the intensity from each underlying state is shown, corrected for light incident at 45° with respect to the spin-orbit quantization axis, as detailed in the Supplementary Information. Error bars represent statistical uncertainty based on number of counts in the Mott polarimeters, plotted at 95% confidence, shown together with locally-weighted scatterplot smoothing fits (Supplementary Information).

$d_{-1_z}^{\downarrow_z}$ ($d_{+1_z}^{\uparrow_z}$) half of the degenerate state will dominate, resulting in an effective \downarrow_z (\uparrow_z) spin polarization. Similarly, photoemission from the higher binding-energy antiparallel state $|d_{-1_z}^{\uparrow_z}, d_{+1_z}^{\downarrow_z}\rangle$ using \oplus (\ominus) light will result in photoemission with the opposite spin polarization, \uparrow_z (\downarrow_z).

When observed with regular spin-integrated ARPES, the energy distribution curve from the Γ point shows both predicted states as a single broad feature with width ~ 400 meV (Supplementary Information); however, by using circularly polarized light and observing the spin-polarization of the photoelectrons, it is possible to distinguish them. The experiment is repeated twice, with both helicities of light, and the results combined to calculate the photoelectron *polarization asymmetry* which eliminates possible experimental artefacts (Supplementary Information). This polarization asymmetry is shown in Fig. S3(a): it is zero for the x and y directions, and shows a clear wiggle as a function of energy in the z direction. The non-zero values indicate that the photoelectrons have a photon-helicity-dependent spin-polarization only in the z -direction, while the binding-energy dependence is due to the origin of the photoelectrons shifting from parallel to antiparallel states. By plotting the intensities corresponding to the observed photoelectron polarization asymmetry for each spatial dimension, Fig. S3(b-d), we can directly resolve these states. In Fig. S3(d), the z direction, they become visible as two energy-split features: $|d_{-1_z}^{\downarrow_z}, d_{+1_z}^{\uparrow_z}\rangle$ is the state that photoemits \downarrow_z with \oplus light and \uparrow_z with \ominus light, i.e. the feature detected in $I_{\oplus\downarrow,\oplus\uparrow}$, whereas $|d_{-1_z}^{\uparrow_z}, d_{+1_z}^{\downarrow_z}\rangle$ is detected in $I_{\oplus\uparrow,\oplus\downarrow}$. Along the x and y directions in Fig. S3(b,c), however, the spectra match the spin-integrated intensity since the photoelectrons from both states have $\langle s_x \rangle = \langle s_y \rangle = 0$ for both helicities of light. The splitting in the z direction is observed with both 24 eV and 56 eV photons and

its magnitude is 130 ± 30 meV (Supplementary Information), showing good agreement or a possible enhancement compared to the predicted SO splitting of $\zeta_{\text{eff}} \sim 90$ meV. Most importantly, the existence of these two states, from which spin-polarized photoemission can be generated using circularly polarized light in the z direction only, is clear experimental evidence of the importance of SO coupling in Sr_2RuO_4 and of its consequences for the complex nature of the normal-state wavefunctions.

As discussed below, the most important of these consequences is the strong, momentum-dependent, spin-orbital entanglement of the eigenstates around the Fermi surface. This is illustrated in Fig. 3 by plotting the projection of the Bloch wavefunctions at the Fermi energy onto the Ru- d orbital basis at different momenta (Methods). The resulting projections are color-coded by the expectation value of the spin operator $\langle s_z \rangle_{(\theta,\phi)}$ for one half of the Kramers-degenerate pair (blue= \uparrow , red= \downarrow). Along the edges of the Brillouin zone (M-X) where the bands are well-separated, we find particularly in the α band (far right panel in Fig. 3) that the orbitals do not show strong entanglement: each orbital projection is associated with a single expectation value (color) of the spin operator. We also notice that in these areas the β and α bands are of pure $d_{xz,yz}$ orbital character, and the γ band of d_{xy} (Fig. 3). At these locations the wavefunction could be well approximated by the usual description as a product of independent spatial and spin components:

$$\psi(\mathbf{k}, \sigma) = \varphi(\mathbf{k}) \phi_\sigma^{\text{spin}}, \quad (1)$$

where $\varphi(\mathbf{k})$ and $\phi_\sigma^{\text{spin}}$ are the spin and orbital eigenstates, and σ the spin index. However, close to the zone diagonal, e.g. near the intersections of the Fermi sheets with Γ -X, this is not the case. Here we find strong orbital mixing for all bands and, especially in the γ and β bands, also strong entanglement between orbital and spin character: the orbitals are no longer associated with a uni-

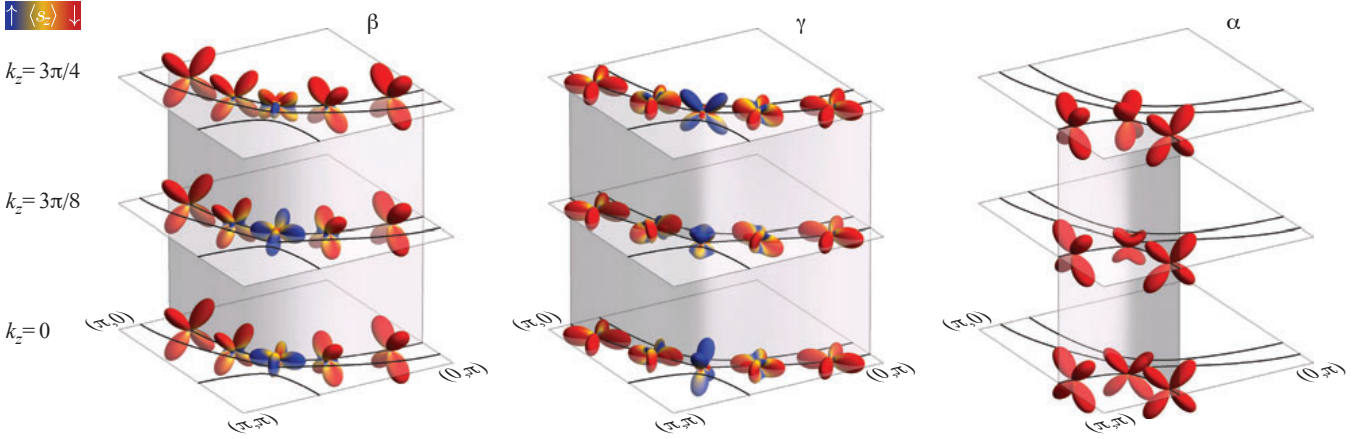


FIG. 3: **Momentum dependent spin-orbital entanglement of the Sr_2RuO_4 eigenstates around the Fermi surface.** Momentum-dependent Ru- d orbital projection of the wavefunction for the β , γ , and α bands at selected momentum locations on the 3D Fermi surface. The surface color represents the momentum-dependent s_z expectation value along the direction defined by the spherical (θ, ϕ) angles, $\langle s_z \rangle_{(\theta, \phi)}$ (see Methods for definition); as indicated by the color scale at upper left, blue/red correspond to spin \uparrow/\downarrow for one state of the Kramers-degenerate pair (with the other state – not shown – having opposite spin polarization, consistent with the absence of net spin polarization at any k point in Sr_2RuO_4). The strongly mixed colors on some of the orbital projection surfaces indicate strong, momentum-dependent spin-orbital entanglement.

form spin value (color) and, on the contrary, the latter can vary from fully up to fully down along a single orbital projection surface. Meaning that, at these locations, the wavefunction cannot be expressed as the product of independent spatial and spin factors; instead, we need the more general expression:

$$\psi(\mathbf{k}, \tilde{\sigma}) = c_{\uparrow} \varphi_{\uparrow}(\mathbf{k}) \phi_{\uparrow}^{\text{spin}} + c_{\downarrow} \varphi_{\downarrow}(\mathbf{k}) \phi_{\downarrow}^{\text{spin}}, \quad (2)$$

with $\tilde{\sigma}$ being the pseudo-spin index, and $c_{\uparrow, \downarrow}$ the prefactors of the momentum-dependent spin-orbital-entangled eigenstates. Eq. 2 further illustrates the nature of the SO-induced entanglement: flipping the spin forces also a change of the orbital character. We note that, due to the nature of the band structure in Sr_2RuO_4 , this entanglement is strongly momentum dependent in both k_{\parallel} and k_z , despite the extremely weak k_z dispersion along the Fermi surface.

A similar momentum and orbital dependence of the spin expectation value is responsible – in topological insulators – for the complex spin-texture of the Dirac fermions [12, 24]. In Sr_2RuO_4 , beyond the normal-state properties, it directly affects the description of superconductivity, as revealed by the inspection of the Cooper pair basic structure. Cooper assumed the two-particle wavefunction describing a superconducting electron pair to be of the form $\Psi(\mathbf{r}_1, \sigma_1, \mathbf{r}_2, \sigma_2) = \varphi(\mathbf{r}_1 - \mathbf{r}_2) \phi_{\sigma_1, \sigma_2}^{\text{spin}}$, with zero total momentum and the spin part being either singlet (total spin $S=0$) or triplet ($S=1$) [25]. This allows one to classify superconductors as a realization of singlet or triplet paired states. However, a fundamental assumption of this description is that one can write the wavefunction of each electron as a simple product of spatial and spin parts, which is not possible in the case of

strong mixing between $\varphi_{\uparrow}(\mathbf{k})$ and $\varphi_{\downarrow}(\mathbf{k})$. Additionally, because of the strong 3D k -dependence of this entanglement in Sr_2RuO_4 , any transform to pseudo-spin would also necessarily be k -dependent – negating the possibility of using the regular description under a pseudo-spin basis as might be done, e.g., when describing superconductivity in the heavy-fermion Ce compounds [26, 27]. As a consequence, the classification of Cooper pairs in terms of singlets or triplets fundamentally breaks down for Sr_2RuO_4 . This is shown in Fig. S5 of the Supplementary Information, which presents the spin-eigenstates available to a pair of electrons with zero total momentum as obtained from the expectation value $\langle \vec{s}_{\mathbf{k}} \cdot \vec{s}_{-\mathbf{k}} \rangle$. While the familiar singlet and triplet states are seen off the zone diagonal for the α band (with $\langle \vec{s}_{\mathbf{k}} \cdot \vec{s}_{-\mathbf{k}} \rangle = -3/4$ and $1/4$, respectively), they are not available for either the β or γ bands, whose spin-eigensystem consists of a doublet and two singlets or – depending on the location in k -space – two doublets.

Our findings mark a deviation from a pure spin-triplet pairing for Sr_2RuO_4 , since the only portion of the Fermi surface that might support it is contained within the α pocket. This could explain a number of experimental observations at variance with a spin-triplet scenario, such as the extreme sensitivity to field angle of both the magnetic-field-induced second superconducting phase transition [7] and also the suppression of the ab -plane upper critical field [8]. These provide evidence for an additional magnetic anisotropy in the superconducting state, of which SO coupling would be the natural source. Our study suggests that the superconductivity in Sr_2RuO_4 is yet more unconventional than has been assumed so far: provided that the pairing interaction is

relatively weak, the entanglement of spin and orbit at the single-particle level becomes an essential feature to take into account when describing the superconducting pairing. In this regard, it would be interesting to verify what of the chiral p -wave superconductor phenomenology [1–5], and apparent conflict in experimental evidence [7–9], would remain when re-evaluated in terms of entangled single-particle eigenstates.

METHODS

Spin-resolved ARPES experiments. The measurements were performed on the normal state of Sr_2RuO_4 at the Swiss Light Source using the COPHEE endstation on the Surface and Interface Spectroscopy beamline, with ~ 100 meV energy resolution and $\sim 1^\circ$ angular resolution (the latter is equivalent to $\sim 0.1\pi/a$ at 24 eV and $\sim 0.2\pi/a$ at 56 eV photon energy), which allows the selection of electrons in energy-momentum space. These electrons are deflected into an array of Mott detectors, where the spin polarization can be resolved in all three spatial dimensions. High-quality Sr_2RuO_4 single crystals with no 3 K phase contamination [28] were cleaved in situ at 40 K and base pressures in the 10^{-9} mbar range. Owing to the relatively high temperature and pressure, no features associated with the reconstructed surface were detected [28]. All measurements were repeated using the beamline’s elliptically-polarizing undulator to generate both right (\oplus) and left (\ominus) circularly polarized light, and the photoelectron polarization asymmetry P^\otimes was calculated using the geometric formula [29] to eliminate the effects of circular dichroism (Supplementary Information):

$$P^\otimes S_{\text{Mott}} = \frac{\sqrt{I_U^\oplus I_D^\ominus} - \sqrt{I_D^\oplus I_U^\ominus}}{\sqrt{I_U^\oplus I_D^\ominus} + \sqrt{I_D^\oplus I_U^\ominus}}. \quad (3)$$

Here S_{Mott} is the empirically determined measure of the efficiency of a Mott spin-detector pair (the so-called Sherman function), and I is the intensity for the up (U) and down (D) halves of the Mott pair measured with circular plus (\oplus) and minus (\ominus) light. This formula was used for each of the Mott polarimeter pairs and the resulting polarization asymmetry was then translated into sample coordinates according to the experimental geometry. With the effects of dichroism eliminated, this photoelectron polarization asymmetry is equivalent to the true energy- and momentum-resolved photon-helicity-dependent electron spin polarization.

Electronic structure calculations. To theoretically study the effects of the SO interaction on the low-energy electronic states of Sr_2RuO_4 , and in particular the momentum-dependent spin-orbital entanglement, the bulk band structure was calculated using the linear muffin-tin orbital (LMTO) code, which was tested against that calculated with full-potential linearized

augmented-plane-wave method using WIEN2k. The parameters were extracted from the LMTO results using the order- N muffin-tin orbital method [30] on the minimal basis of oxygen $2p$ and ruthenium $4d$ orbitals. Atomic SO coupling was then added as a local term in the Hamiltonian, the results of which show excellent agreement with the Fermi surface and band dispersion obtained from relativistic (i.e., SO included) calculations in WIEN2k. The orbitals in Fig. 3 depict the (θ, ϕ) angular dependence of the Ru- d orbital projection of the Bloch wavefunctions for a given momentum at the Fermi energy. Shown is the surface defined by the equation $r(\theta, \phi) = \sum_{\tau, \tau'} Z_\tau(\theta, \phi) Z_{\tau'}(\theta, \phi) \langle a_{i, \tau, k}^\dagger a_{i, \tau', k} \rangle$, where i and τ are the band and Ru- d orbital indexes, k is the momentum of the Bloch eigenstate, and Z are the cubic harmonics. The surface color corresponds to the momentum-dependent s_z expectation value along the direction defined by the spherical (θ, ϕ) angles, $\langle s_z \rangle_{(\theta, \phi)} = \sum_{\tau, \tau'} Z_\tau(\theta, \phi) Z_{\tau'}(\theta, \phi) \frac{1}{2} \langle a_{i, \tau, k, \uparrow}^\dagger a_{i, \tau, k, \uparrow} - a_{i, \tau, k, \downarrow}^\dagger a_{i, \tau, k, \downarrow} \rangle$, with only one of the Kramers degenerate states shown.

ACKNOWLEDGEMENTS

We gratefully acknowledge A. Kapitulnik, W.A. MacFarlane, G.A. Sawatzky, P.C.E. Stamp, and L.H. Tjeng for discussions. This work was supported by the Max Planck - UBC Centre for Quantum Materials (A.N., M.W.H.), the Killam, Alfred P. Sloan, Alexander von Humboldt, and NSERC’s Steacie Memorial Fellowship Programs (A.D.), the Canada Research Chairs Program (A.D.), NSERC, CFI, CIFAR Quantum Materials, MEXT KAKENHI (No. 22103002), and the Deutsche Forschungsgemeinschaft through Forschergruppe FOR 1346.

SUPPLEMENTARY INFORMATION

Components of $\langle \vec{l} \cdot \vec{s} \rangle$ around the Fermi surface

In order to investigate the coupling between the spin and orbital angular momentum near the Fermi energy in Sr_2RuO_4 we plot the expectation value of their dot product, $\langle \vec{l} \cdot \vec{s} \rangle$, for the states around the Fermi surface sheets. In a system without spin-orbit (SO) coupling, the independence of these two vectors would cause this expectation value to be zero everywhere. In Fig. S1(b) we show $\langle \vec{l} \cdot \vec{s} \rangle$, contrasted against the orbital character in (a), as presented in the main text. In (a) we see how the β and α bands are of mostly d_{xz} and d_{yz} character, while the γ band is of mostly d_{xy} character; the exception is near the anticrossing of the β and γ bands close to $(\frac{2\pi}{3}, \frac{2\pi}{3})$ where the strongest mixing occurs and their orbital character changes. In (b) we see that, despite

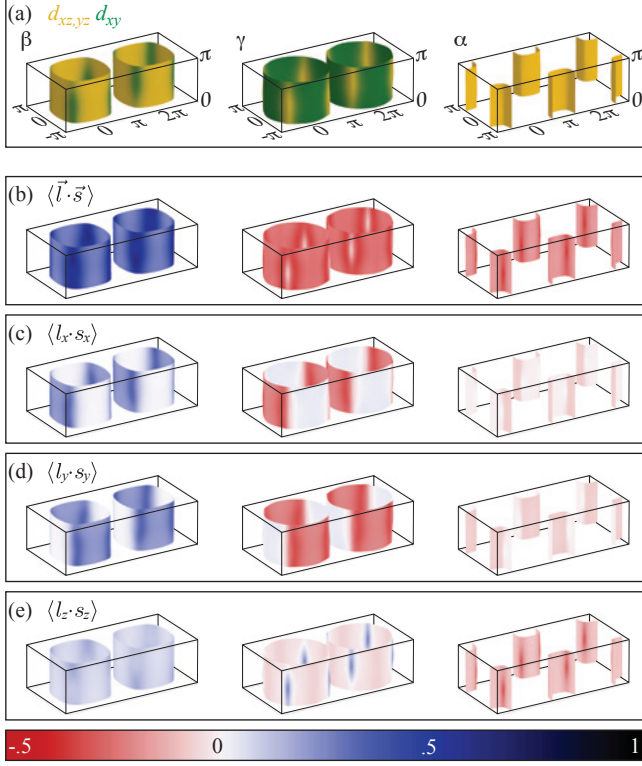


FIG. S1: The Fermi surface sheets of Sr_2RuO_4 colorized to show (a) orbital character, as well as (b) $\langle \vec{l} \cdot \vec{s} \rangle$ and its components (c-e) along the three crystal axes (for the latter the color scale is shown at the bottom). The extended zone scheme is used to illustrate the conventional Brillouin zone in the fundamentally body-centered tetragonal unit cell.

the apparent mixing only at the anticrossing noted in (a), spin and orbital angular momentum remain coupled around almost the entire Fermi surface, as evidenced by the non-zero value of $\langle \vec{l} \cdot \vec{s} \rangle$. Interestingly, we find that $\langle \vec{l} \cdot \vec{s} \rangle = 0$ only near the small portion of the γ band which is of d_{xz}/d_{yz} character. However, in (c-e) we see that this is not because spin and orbit are independent at this location in momentum space; instead we see, in (e) for the z direction especially, that \vec{l} and \vec{s} are just as strongly coupled in this location but that $\langle \vec{l} \cdot \vec{s} \rangle = 0$ only as a sum of non-zero components. This demonstrates that the spin and orbital angular momentum are coupled everywhere on the Fermi surface, for all three $\text{Ru-}t_{2g}$ conduction bands.

High resolution ARPES data

In addition to the spin-resolved data presented in the main text, higher-resolution angle-resolved photoemission spectroscopy (ARPES) experiments were performed at the University of British Columbia. In Fig S2 we present some of this data taken at 5.2 K, under vac-

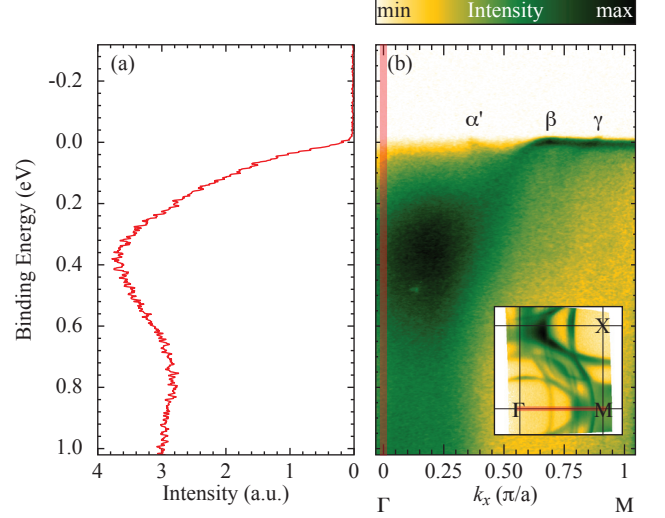


FIG. S2: ARPES on Sr_2RuO_4 at the Γ point; (a) shows an EDC integrated over $\sim 0.03 \frac{\pi}{a}$ around the Γ point, as marked in the band map of panel (b). In (b) bands are labelled as they cross the Fermi level (with primes denoting reconstructed features [28]); the location of the band map shown in the inset.

uum with pressure in the 10^{-11} mbar range, using the 21.22 eV He I spectral line, and resolutions of ~ 17 meV and $\sim 0.01 \frac{\pi}{a}$ angular equivalent. Fig S2(a) shows an energy distribution curve (EDC) taken at the exact same spot in 2D momentum space as that measured with spin-ARPES and presented in the main text, while Fig S2(b) shows its location in momentum space on the measured band map and Fermi surface. This data demonstrates that the two states studied by spin-ARPES and presented in the main text have a fundamentally broad lineshape – even with a resolution approximately seven times smaller than the splitting their separation cannot be resolved without circularly polarized light and spin discrimination. Note that this sample, cleaved at lower temperature and in better vacuum conditions, shows clear evidence of the reconstructed surface electronic structure [19, 28] (as seen by the folded α' band), while that presented in the main text did not. In either case no additional folded features will appear in the studied EDC at the Γ point, owing to the nature of the folding which maps the X point (which has no features in that energy range) to the Γ point – an additional benefit of performing the experiment at this location in momentum space.

Polarization asymmetry and the angle of incidence in spin-ARPES

The geometric polarization asymmetry [29], defined as in the main text in terms of the intensities (I) from the up (U) and down (D) detectors for circular right (\oplus) and

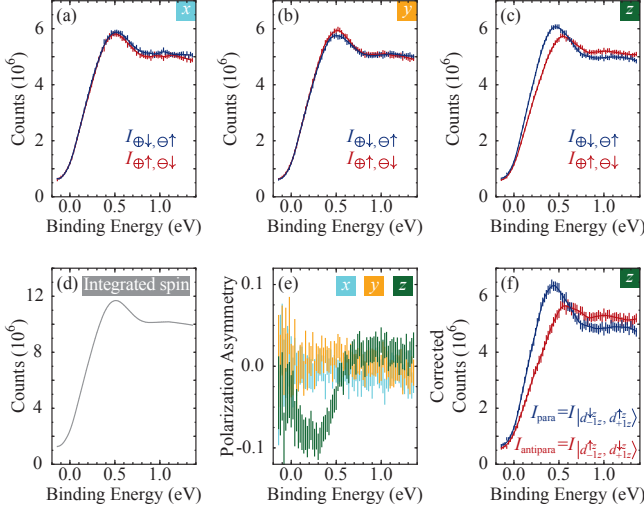


FIG. S3: Spin-ARPES using 24eV circularly polarized light on Sr_2RuO_4 at the Γ point. (a-c) Spin-ARPES intensities relative to each of the crystal axes obtained with right (\oplus) or left (\ominus) circularly polarized light; these are derived, according to Eq. S7, from the integrated spin data and measured polarization asymmetry shown in panel (d) and (e). (f) Intensity from each underlying state, corrected for light incident at 45° with respect to the spin-orbit quantization axis and assuming no background, according to Eq. S9. Error bars represent statistical uncertainty based on number of counts in the Mott Polarimeters, plotted at 95% confidence, with locally weighted scatterplot smoothing fits shown [31].

left (\ominus) light, is given by the following expression:

$$P^\otimes S_{\text{Mott}} = \frac{\sqrt{I_U^\oplus I_D^\ominus} - \sqrt{I_D^\oplus I_U^\ominus}}{\sqrt{I_U^\oplus I_D^\ominus} + \sqrt{I_D^\oplus I_U^\ominus}}, \quad (\text{S4})$$

which eliminates the effects of circular dichroism and any response imbalance that might exist between the two detectors in the Mott pair (the Sherman “function”, S_{Mott} , is a measure of the efficiency of spin discrimination and is a constant, which we ignore here for simplicity). The effectiveness of Eq. S4 can be seen by modelling the measured intensities as:

$$\begin{aligned} I_U^\oplus &= d^\oplus r_U I_{\oplus\uparrow,\ominus\downarrow} \\ I_D^\ominus &= d^\ominus r_D I_{\oplus\uparrow,\ominus\downarrow} \\ I_D^\oplus &= d^\oplus r_D I_{\oplus\downarrow,\ominus\uparrow} \\ I_U^\ominus &= d^\ominus r_U I_{\oplus\downarrow,\ominus\uparrow}. \end{aligned} \quad (\text{S5})$$

Here the d and r terms account for the circular dichroism and detector response rates and $I_{\oplus\uparrow,\ominus\downarrow} \equiv I_{\oplus\uparrow} = I_{\ominus\downarrow}$ (and its opposite, $I_{\oplus\downarrow,\ominus\uparrow}$) are the fundamental photoemission intensities we are interested in, whose spin polarization changes sign upon switching the helicity of the incident light. By substitution we see that the dichroism and detector efficiencies cancel out, and the polarization

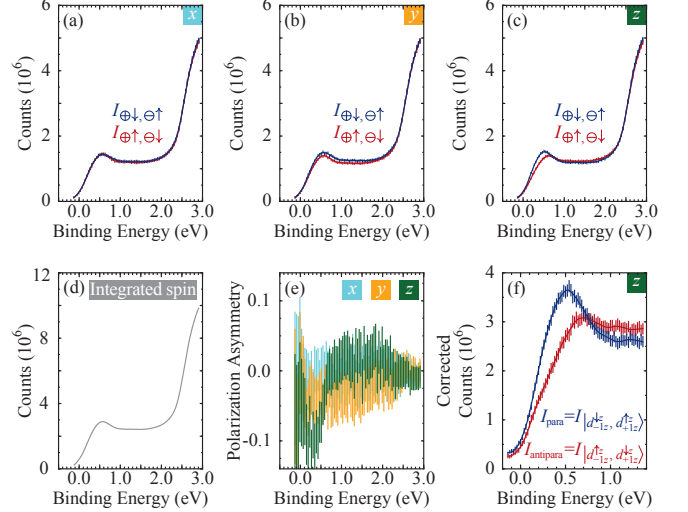


FIG. S4: Spin-ARPES using 56eV circularly polarized light on Sr_2RuO_4 at the Γ point, and taken over a larger energy range than Fig. S3; this wider range shows that the polarization asymmetry goes to zero at the non-SO split higher binding-energy states. (a-c) Spin-ARPES intensities relative to each of the crystal axes obtained with right (\oplus) or left (\ominus) circularly polarized light; these are derived, according to Eq. S7, from the integrated spin data and measured polarization asymmetry shown in panel (d) and (e). (f) Close-up in energy of the intensity from each underlying state, corrected for light incident at 45° with respect to the spin-orbit quantization axis and assuming no background, according to Eq. S9; this panel is taken from an additional data set with narrower energy binning. Error bars represent statistical uncertainty based on number of counts in the Mott Polarimeters, plotted at 95% confidence, with locally weighted scatterplot smoothing fits shown [31].

asymmetry reverts to the simple form:

$$P^\otimes = \frac{I_{\oplus\uparrow,\ominus\downarrow} - I_{\oplus\downarrow,\ominus\uparrow}}{I_{\oplus\uparrow,\ominus\downarrow} + I_{\oplus\downarrow,\ominus\uparrow}}. \quad (\text{S6})$$

The total intensity (I_T) can thus be combined with the measured polarization asymmetry to reconstruct the spin intensities for each spatial direction according to:

$$\begin{aligned} I_{\oplus\uparrow,\ominus\downarrow} &= I_T(1 + P^\otimes)/2 \\ I_{\oplus\downarrow,\ominus\uparrow} &= I_T(1 - P^\otimes)/2. \end{aligned} \quad (\text{S7})$$

These are the spin intensities shown in Figs. S3(a-c) and S4(a-c) for the two measured photon energies of 24 and 56 eV, as constructed directly from the integrated spin (d) and polarization asymmetry (e). From these datasets two distinct features, split in the z direction only, are already apparent (we also note that, while similar in all respects, the wider binding energy range 56 eV data show that the polarization asymmetry vanishes at the non-SO split, high-energy oxygen states). However, owing to the experimental geometry (light incident at 45° relative to the analyzer), photons cannot be incident directly along

the z direction (additionally there is a node in the final state preventing the experiment from being performed in the second Brillouin zone with normal incident light and 45° emission). The result is that with equal probability the photons will interact either with m_{l_z} , resulting in spin-polarized photoemission from the states with parallel and antiparallel spin and orbital angular momentum (as described in the main text), or with m_{l_x} , resulting in non-polarized photoemission from both states (which will be measured as either \uparrow or \downarrow with equal probability). Therefore, in the z direction, the spin intensity measured for each configuration in terms of these underlying states will be given by:

$$\begin{aligned} I_{\oplus\downarrow,\oplus\uparrow} &= \frac{I_{\text{parallel}}}{2} + \frac{I_{\text{parallel}}}{4} + \frac{I_{\text{antiparallel}}}{4} \\ I_{\oplus\uparrow,\oplus\downarrow} &= \frac{I_{\text{antiparallel}}}{2} + \frac{I_{\text{antiparallel}}}{4} + \frac{I_{\text{parallel}}}{4}. \end{aligned} \quad (\text{S8})$$

Here I_{parallel} and $I_{\text{antiparallel}}$ represent the total photoemission intensity given off by the states discussed in the main text; the single terms on the left represent the spin-polarized photoemission described in the main text (divided by two due to only half of the photons interacting with m_{l_z}), while the two terms on the right represent the non-spin-polarized photoemission (divided by four due to half photons interacting with m_{l_x} , and half of those being measured as either up or down). This dilution causes a decrease in the observed splitting compared to the intrinsic one, which can be corrected by taking

$$\begin{aligned} I_{\text{parallel}} &= (3I_{\oplus\downarrow,\oplus\uparrow} - I_{\oplus\uparrow,\oplus\downarrow})/2 = I_T(1 - 2P^\otimes)/2 \\ I_{\text{antiparallel}} &= (3I_{\oplus\uparrow,\oplus\downarrow} - I_{\oplus\downarrow,\oplus\uparrow})/2 = I_T(1 + 2P^\otimes)/2 \end{aligned} \quad (\text{S9})$$

to recover the intensities from each state; this assumes that all observed intensity is from only these two states with no background. Such a correction is shown in Fig. S3(f) and S4(f), as well as Fig. 2(d) of the main text, and returns a larger splitting.

Observing the uncorrected splitting at the different photon energies and energy ranges measured results in estimates of 83 meV, 101 meV, and 110 meV for an average of 98 ± 14 meV. However, this estimate *must* be low due to the experimental geometry and its effect as described above. Using the correction, as described above, on the same data sets results in estimates of 125 meV, 184 meV, and 172 meV for an average of 160 ± 30 meV. However, this estimate *may* be high, as it assumes that all intensity arises from these two states with no background. These limits therefore represent upper and lower bounds of the intrinsic splitting between these two states, for an overall estimate of 130 ± 30 meV.

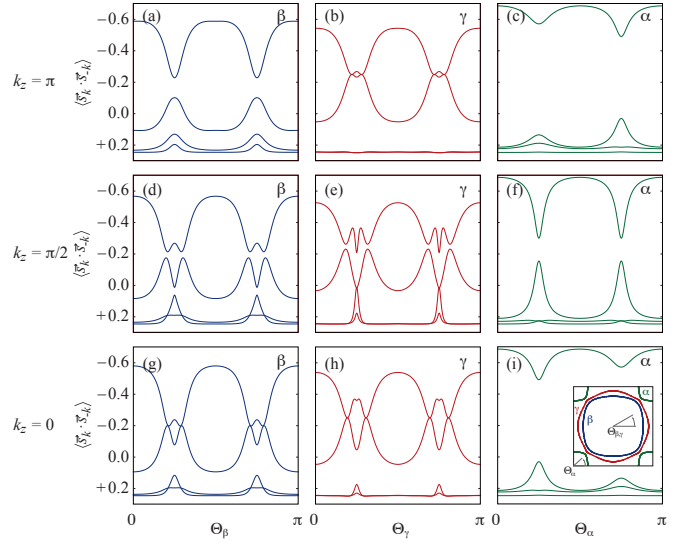


FIG. S5: $\langle \vec{s}_k \cdot \vec{s}_{-k} \rangle$ between two states with opposite momentum on the Fermi surface sheets in Sr_2RuO_4 for the β (a,d,g), γ (b,e,h), and α (c,f,i) bands at $k_z = 0$ (g-i), $\frac{\pi}{2}$ (d-f), and π (a-c). The location in the k_x-k_y plane is defined by the angle Θ for each band, as illustrated in the inset at lower right.

Available spin-eigenstates around the Fermi surface

Thus far we have examined only single-particle properties, however, without making any assumptions about the pairing mechanism, we may also use our model to examine the spin-eigenstates available to a pair of electrons with 0 net momentum – one electron at k and one at $-k$. These eigenstates are shown in Fig. S5 by plotting the expectation value of $\vec{s}_k \cdot \vec{s}_{-k}$ around the Fermi surface sheets for all bands at three k_z values. Pure, uncoupled, spins will form the familiar singlet/triplet eigensystem, which is visible at a single state with $\langle \vec{s}_k \cdot \vec{s}_{-k} \rangle = -\frac{3}{4}$ and a triplet of states with $\langle \vec{s}_k \cdot \vec{s}_{-k} \rangle = \frac{1}{4}$; such a system can be seen to occur off the zone diagonal for the α band in Fig. S5(c,f,i). However, a singlet/triplet eigensystem is not available for either the β or γ bands anywhere in momentum space, as seen in Fig. S5(a,d,g) and (b,e,h), respectively; instead the available eigensystem is observed to be either a doublet and two singlets, or two doublets, depending on the location in k -space. In this regard, we also note that the introduction of a momentum-dependent pseudo-spin would not resolve this issue, since the unitary transformation $\tilde{\sigma} = \mathcal{U}(\mathbf{k})\sigma$ that in a momentum-dependent fashion links the spin and pseudo-spin for the one-particle eigenstates also enters in the spin operator, $\tilde{s} = \mathcal{U}^\dagger(\mathbf{k})s\mathcal{U}(\mathbf{k})$, thereby leaving the expectation values unaltered.

-
- * Electronic address: damascelli@physics.ubc.ca
- [1] Luke, G. M. *et al.* Time-reversal symmetry-breaking superconductivity in Sr_2RuO_4 . *Nature* **394**, 558–561 (1998).
 - [2] Riseman, T. M. *et al.* Observation of a square flux-line lattice in the unconventional superconductor Sr_2RuO_4 . *Nature* **396**, 242–245 (1998).
 - [3] Ishida, K. *et al.* Spin-triplet superconductivity in Sr_2RuO_4 identified by ^{17}O Knight shift. *Nature* **396**, 658–660 (1998).
 - [4] Nelson, K. D., Mao, Z. Q., Maeno, Y. & Liu, Y. Odd-Parity Superconductivity in Sr_2RuO_4 . *Science* **306**, 1151–1154 (2004).
 - [5] Xia, J., Maeno, Y., Beyersdorf, P. T., Fejer, M. M. & Kapitulnik, A. High Resolution Polar Kerr Effect Measurements of Sr_2RuO_4 : Evidence for Broken Time-Reversal Symmetry in the Superconducting State. *Phys. Rev. Lett.* **97**, 167002 (2006).
 - [6] Rice, M. Superconductivity: An analogue of superfluid ^3He . *Nature* **396**, 627–629 (1998).
 - [7] Mao, Z. Q., Maeno, Y., NishiZaki, S., Akima, T. & Ishiguro, T. In-plane anisotropy of upper critical field in Sr_2RuO_4 . *Phys. Rev. Lett.* **84**, 991–994 (2000).
 - [8] Kittaka, S. *et al.* Angular dependence of the upper critical field of Sr_2RuO_4 . *Phys. Rev. B* **80**, 174514 (2009).
 - [9] Yonezawa, S., Kajikawa, T. & Maeno, Y. First-order superconducting transition of Sr_2RuO_4 . *Phys. Rev. Lett.* **110**, 077003 (2013).
 - [10] Maeno, Y., Kittaka, S., Nomura, T., Yonezawa, S. & Ishida, K. Evaluation of spin-triplet superconductivity in Sr_2RuO_4 . *Journal of the Physical Society of Japan* **81**, 011009 (2012).
 - [11] Haverkort, M. W., Elfimov, I. S., Tjeng, L. H., Sawatzky, G. A. & Damascelli, A. Strong spin-orbit coupling effects on the fermi surface of Sr_2RuO_4 and Sr_2RhO_4 . *Phys. Rev. Lett.* **101**, 026406 (2008).
 - [12] Hasan, M. & Kane, C. Colloquium: Topological insulators. *Rev. Mod. Phys.* **82**, 3045–3067 (2010).
 - [13] Kim, B. J. *et al.* Novel $J_{\text{eff}} = 1/2$ Mott State Induced by Relativistic Spin-Orbit Coupling in Sr_2IrO_4 . *Phys. Rev. Lett.* **101**, 076402 (2008).
 - [14] Comin, R. *et al.* Sr_2IrO_4 as a Novel Relativistic Mott Insulator with a 340-meV Gap. *Phys. Rev. Lett.* **109**, 266406 (2012).
 - [15] Ng, K. K. & Sigrist, M. The role of spin-orbit coupling for the superconducting state in Sr_2RuO_4 . *Europhys. Lett.* **49**, 473 (2000).
 - [16] Raghu, S., Kapitulnik, A. & Kivelson, S. A. Hidden quasi one-dimensional superconductivity in Sr_2RuO_4 . *Phys. Rev. Lett.* **105**, 136401 (2010).
 - [17] Deisz, J. J. & Kidd, T. E. Quantum many-body calculation of mixed-parity pairing in the Sr_2RuO_4 superconductor induced by spin-orbit coupling. *Phys. Rev. Lett.* **107**, 277003 (2011).
 - [18] Puetter, C. M. & Kee, H.-Y. Identifying spin-triplet pairing in spin-orbit coupled multi-band superconductors. *EPL* **98**, 27010 (2012).
 - [19] Damascelli, A. *et al.* Fermi surface, surface states, and surface reconstruction in Sr_2RuO_4 . *Phys. Rev. Lett.* **85**, 5194–5197 (2000).
 - [20] Iwasawa, H. *et al.* Interplay among coulomb interaction, spin-orbit interaction, and multiple electron-boson interactions in Sr_2RuO_4 . *Phys. Rev. Lett.* **105**, 226406 (2010).
 - [21] We also note that $\langle \vec{l} \cdot \vec{s} \rangle = 0$ does not necessarily imply that SO coupling is not important; while the eigenstates may still be entangled, the individual $\vec{l} \cdot \vec{s}$ vector components might simply sum to zero, as is the case for the bulges of the γ band near the zone diagonals (see Supplementary Information).
 - [22] Pierce, D. T. & Meier, F. Photoemission of spin-polarized electrons from GaAs. *Phys. Rev. B* **13**, 5484–5500 (1976).
 - [23] Mizokawa, T. *et al.* Spin-orbit coupling in the mott insulator Ca_2RuO_4 . *Phys. Rev. Lett.* **87**, 077202 (2001).
 - [24] Zhu, Z.-H. *et al.* Layer-by-layer entangled spin-orbital texture of the topological surface state in Bi_2Se_3 . *arXiv:1212.4845* (2012).
 - [25] Bardeen, J., Cooper, L. N. & Schrieffer, J. R. Theory of superconductivity. *Phys. Rev.* **108**, 1175–1204 (1957).
 - [26] Mukuda, H. *et al.* Spin susceptibility of noncentrosymmetric heavy-fermion superconductor CeIrSi_3 under pressure: ^{29}Si knight-shift study on single crystal. *Phys. Rev. Lett.* **104**, 017002 (2010).
 - [27] In heavy-fermion compounds the SO coupling is much larger than the bandwidth, suppressing the momentum dependence of the pseudo-spin transform and enabling a pseudo-spin description of superconductivity.
 - [28] Veenstra, C. N. *et al.* Determining the Surface-To-Bulk Progression in the Normal-State Electronic Structure of Sr_2RuO_4 by Angle-Resolved Photoemission and Density Functional Theory. *Phys. Rev. Lett.* **110**, 097004 (2013).
 - [29] Osterwalder, J. Spin-polarized photoemission. *Lect. Notes Phys.* **697**, 95 (2006).
 - [30] Andersen, O. K. & Saha-Dasgupta, T. Muffin-tin orbitals of arbitrary order. *Phys. Rev. B* **62**, R16219 (2000).
 - [31] Cleveland, W. Robust locally weighted regression and smoothing scatterplots. *Journal of the American Statistical Association* **74**, 829–836 (1979).